Effect of Cyclic Flange Local Buckling on the Capacity of Steel Members

Tung-Yu Wu[a,*]; Sherif El-Tawil[b]; and Jason McCormick[b]

[a] Department of Civil Engineering, National Taiwan University, Taipei, 10617, Taiwan

[b] Department of Civil and Environmental Engineering, University of Michigan, Ann Arbor, MI 48109, United States

ABSTRACT

Cyclic flange local buckling typically occurs when plastic hinges form in the beams and columns of special moment resisting frames subject to seismic excitation. While local buckling in beam plastic hinges has been investigated in the past for monotonic loading situations, the effect of cyclic flange local buckling on beam and column behaviors is not yet well understood. In order to address this shortcoming, nineteen half-scale T-section specimens are tested under cyclic axial loads in a configuration intended to replicate the cyclic demands imposed on flanges of beams and columns in their plastic hinge region. The main experimental variables are flange slenderness ratio, level of web restraint, and loading scheme (monotonic versus cyclic). Validated computational studies are performed to expand the parameter space. The test data and computational results show that T-section members that meet the current highly ductile limit can suffer excessive axial strength degradation under cyclic axial loading. The effect of slenderness ratios on column compression capacity due to strength degradation of flanges is evaluated and quantified.

Keywords: cyclic response; local instability; steel structures; capacity; seismic loading

---

[*] Corresponding author at: Department of Civil Engineering, National Taiwan University, Taipei, 10617, Taiwan. Tel.: +886 2 3366 4248. E-mail address: tungyuwu@ntu.edu.tw (T.-Y Wu)

1. Introduction

Local buckling can cause significant strength and stiffness degradation in steel member response during an earthquake. Maximum values for the slenderness ratios of unstiffened and stiffened elements of wide flange sections (i.e. $b/2t_f$ for flanges and h/t_w for webs, where b_f and h are flange width and web height, respectively, and t_f and t_w are flange and web thicknesses, respectively) are specified in the AISC specifications [1]. When ductility is important, e.g. in earthquake applications, the maximum slenderness ratios are specified in the AISC seismic provisions [2] for members classified as highly ductile or moderately ductile. The current slenderness limits are derived from early analytical and experimental research on beams under monotonic loading [3-6].

Information on the effect of cyclic loading on the slenderness limits is rather rare in the literature and is typically inferred from member level response. Richards and Uang [7] studied the effect of flange slenderness ratio on the cyclic rotation capacity of links using finite element models. Their results suggested that the existing limiting slenderness ratios for link flanges could be relaxed. Newell and Uang [8] conducted cyclic tests of W14 columns subjected to axial forces combined with large drift loading. The stocky webs of W14 columns were found to stabilize the flange and contribute to the observed large deformation capacity of the studied sections. Cheng et al. [9] tested nine H-shaped beam-columns with large slenderness ratios and concluded that the effect of flange/web slenderness ratios and axial force ratios should be considered mutually because of their strong dependence upon each other. The computational study performed by Elkady and Lignos [10] indicated that current limiting ratios for highly ductile members are not adequate for columns subjected to a constant axial load of $0.2P_y$ or more, where P_y is the axial yield strength of the cross section. Fogarty and El-Tawil [11], Fogarty et al. [12] and Wu et al. [13] reached similar conclusions and proposed revised highly ductile limits for deep columns.

The intent of this paper is to address the paucity of experimental data on the effect of flange local buckling (FLB) and develop a deeper understanding of the effect of the FLB slenderness on the cyclic response of steel wide flange sections. To this end, nineteen half-scale T-section specimens are subjected to monotonic axial compression and cyclic axial loading. The test configuration and axial loading protocols are carefully chosen and developed to replicate the seismic demands imposed on beam flanges and column flanges in their plastic hinge regions. The specimens cover a wide range of flange slenderness ratios and allow for the study of the effect of web restraint on flange local buckling behavior. A computational study is performed to further investigate the effect of local slenderness ratios on the cyclic behavior of column flanges. The peak strength and strength degradation rates observed from the test and simulations are compared and used to evaluate current seismic provisions for local instability of steel members.

2. Finite Element Model Development and Validation

The finite element models employed in this work are created and analyzed using the commercial software, Hypermesh [14] and LS-DYNA [15], respectively. The models are discretized using 4-node fully integrated shell elements (ELFORM 16) based on the formulation published by Engelmann et al. [16] with a mesh size of 25.4 mm, which is also employed in Fogarty and El-Tawil [11]. The mesh density is kept constant in all models to avoid mesh size dependency. A combined isotropic/kinematic hardening material model (MAT_153) developed by Huang and Mahin [17] is assigned to the shell elements. The hardening moduli and model parameters are calibrated to the true stress-true strain model proposed by Arasaratnam et al. [18] using nominal properties of A992 steel. Initial imperfections in the T-section members used herein are obtained by applying the first buckling mode as a geometric perturbation. Calibration studies showed that the results match the test data best when the maximum amplitude of the applied perturbation geometry is the plate width divided by 500. For example, for a flange with a width of 152.4 mm, the magnitude of its imperfection is 0.305 mm. The modeling approach has been extensively validated in previous work by the authors, e.g. in Fogarty and El-Tawil [11], Fogarty et al. [12] and Wu et al. [19]. Additional validation studies using the experimental data obtained in this work are discussed later on in the paper.

3. Rationale for T-Section Test Specimens

Under seismic loading, structural members of a special moment frame (SMF), such as beams and columns, are subjected to either cyclic bending moment or combined cyclic axial force and bending moment in their plastic hinge regions. The premise of this paper is that the seismic demands on flanges in the plastic hinge region can be approximated as cyclic axial deformation demands for wide flange beams and columns, as shown in Fig. 1. Therefore, rather than testing a complete structural component or subassemblage, a short T-section column with fixed ends can be tested under cyclic axial loading instead. This assumption substantially simplifies the study of inelastic cyclic FLB because a hydraulic axial load frame can be used instead of a more comprehensive and complicated setup needed to test a structural member or sub-assembly under cyclic loading.

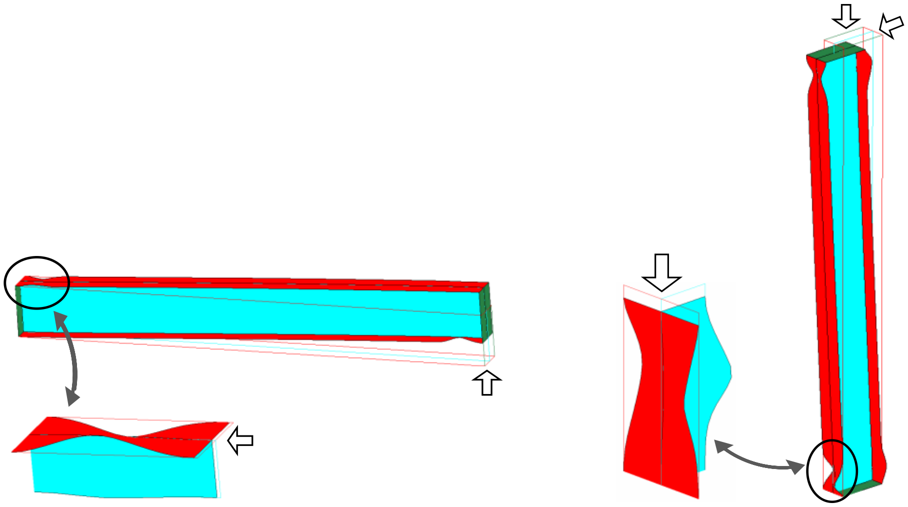
(a) (b)

Fig. 1. Flange deformed shape in plastic hinge region of (a) wide flange beams under cyclic bending moment and (b) wide flange columns under combined cyclic axial force and bending moment.

To ensure that the proposed T-section members realistically represent their full section counterparts, the web portion of the T must be adequately long to impose the same level of flange restraint achieved in the original section. Detailed finite element studies of W24 sections are conducted to determine a reasonable web length. The axial deformation history of the flange in the plastic hinge region, whose length is the same as the section depth as usually assumed [20], is extracted and applied to its counterpart T-section member. The responses of the T-section member and the corresponding portion in the full member are compared in terms of overall deformed shape and the force versus deformation history. The studies suggest that a web length equal to one third of the full section depth results in a meaningful representation of the overall section's behavior.

Fig. 2 shows comparisons between the full and T-section member responses for two different W24 sections under different levels of axial loading. Here, the effective stress ratio (ESR) is defined as the axial strength normalized by the yield strength of the cross-section, i.e. P/P_y, and the normalized axial deformation (NAD) is calculated by Δ/L, where Δ is the relative axial displacement between member's ends and L is the original length of the members. The ESR is used as the performance parameter and represents the retained axial strength of the T-section member after experiencing a given axial deformation history, while the NAD is used to describe the overall status of the members. In Fig. 2, the full members are adapted from Fogarty et al. [12] and are subjected to the symmetric cyclic drift loading used to qualify beam-to-column moment connections in the AISC seismic provisions [2]. It is clear that the overall buckled shape and force deformation history match reasonably well. These results are quite typical and are observed for other W24 sections subjected to different levels of axial load and other types of loading histories including monotonic and the ratcheting history associated with collapse, as discussed in Wu et al. [13].

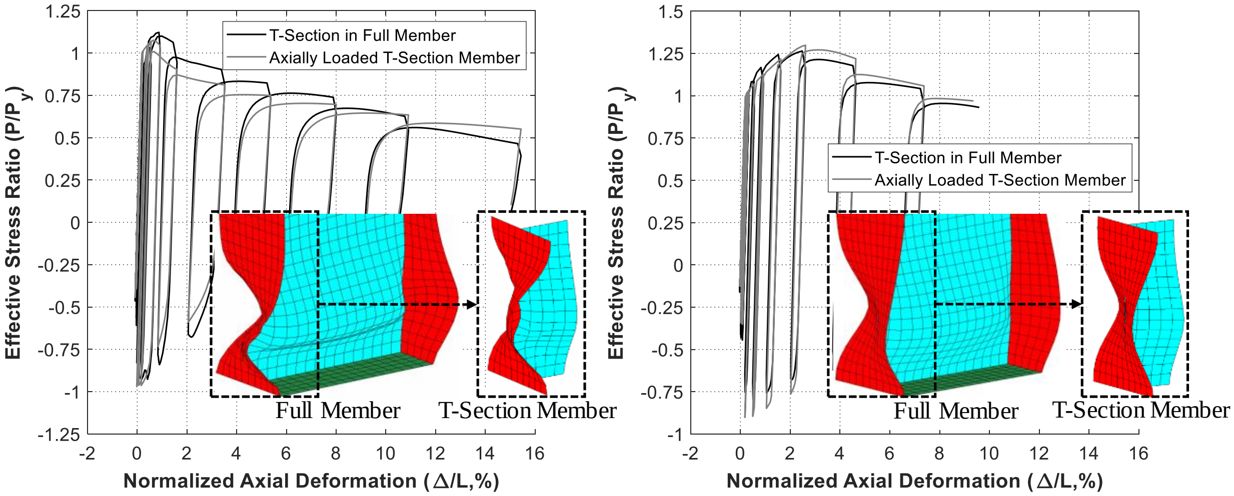

(a) W24×104, $P/P_y = 0.2$ (b) W24×176, $P/P_y = 0.4$

Fig. 2. Comparison between full member and T-section member responses under symmetric drift loading with different axial load levels.

4. Testing Program

4.1 Test specimens and setup

Nineteen half-scale T-section specimens with a depth of 305 mm were selected to represent the behavior of a W24 section, which is commonly used for beams and columns in the current design

Table 1. Test matrix.

Specimen ID	b (mm)	$d/3$ (mm)	t_f (mm)	t_w (mm)	$b/2t_f$	$(h/t_w)_{eq}$	Material (Batch)	Loading Protocol	Buckled Shape	ESR at 4% Beam Drift	ESR at 4% Column Drift
W12×26-CB	164.8	101.6	9.7	5.8	8.54	47.2	A992 (1)	CB	Asym.	0.71	N/A[a]
F1W1-M	152.4	101.6	19.1	9.5	4.0	28.0	A572 (1)	M	Sym.	1.16	1.04
F2W1-M	152.4	101.6	12.7	9.5	6.0	29.3	A572 (1)	M	Asym.	1.18	0.86
F2W1-CB	152.4	101.6	12.7	9.5	6.0	29.3	A572 (1)	CB	Asym.	0.85	N/A[a]
F2W1-CC	152.4	101.6	12.7	9.5	6.0	29.3	A572 (1)	CC	Sym.	N/A[a]	0.78
F4W1-M	152.4	101.6	7.9	9.5	9.6	30.3	A572 (1)	M	Asym.	0.79	0.62
F5W1-M	152.4	101.6	4.8	9.5	16.0	31.0	A572 (1)	M	Asym.	0.73	0.53
F5W1-CB	152.4	101.6	4.8	9.5	16.0	31.0	A572 (1)	CB	Asym.	0.62	N/A[a]
F5W1-CC	152.4	101.6	4.8	9.5	16.0	31.0	A572 (1)	CC	Asym.	N/A[a]	0.49
F1W2-M	152.4	101.6	19.1	6.4	4.0	42.0	A572 (2)	M	Sym.	1.12	0.91
F3W2-M	152.4	101.6	9.5	6.4	8.0	45.0	A572 (1)	M	Asym.	0.79	0.62
F3W2-CB	152.4	101.6	9.5	6.4	8.0	45.0	A572 (2)	CB	Asym.	0.73	N/A[a]
F2W3-M	152.4	101.6	12.7	4.8	6.0	58.7	A572 (1)	M	Sym.	1.08	0.70
F2W3-CB	152.4	101.6	12.7	4.8	6.0	58.7	A572 (2)	CB	Sym.	0.68	N/A[a]
F2W3-CC	152.4	101.6	12.7	4.8	6.0	58.7	A572 (1)	CC	Sym.	N/A[a]	0.51
F4W3-M	152.4	101.6	7.9	4.8	9.6	60.7	A572 (2)	M	Asym.	0.79	0.63
F5W3-M	152.4	101.6	4.8	4.8	16.0	62.0	A572 (1)	M	Asym.	0.59	0.45
F5W3-CB	152.4	101.6	4.8	4.8	16.0	62.0	A572 (1)	CB	Asym.	0.53	N/A[a]
F5W3-CC	152.4	101.6	4.8	4.8	16.0	62.0	A572 (1)	CC	Asym.	N/A[a]	0.44

[a] Not available because the loading protocol is intended to approximate the seismic demands on flanges in beams (columns).

Table 2. Limiting slenderness ratios for flanges and webs.

Description of element	Local slenderness ratio	Limiting width-to-thickness ratio		
		λ_r[a] (nonslender)	λ_{md}[b] (moderately ductile)	λ_{hd}[b] (highly ductile)
Flanges of rolled I-shaped sections	b/t	$0.56\sqrt{E/F_y}$	$0.40\sqrt{\mathrm{E}/\mathrm{R}_y\mathrm{F}_y}$	$0.32\sqrt{E/R_yF_y}$
Flanges of built-up I-sections	b/t	$0.64\sqrt{k_cE/F_y}$ $0.35 \le k_c \le 0.76$ where $k_c = 4/\sqrt{h/t_w}$	$0.40\sqrt{\mathrm{E}/\mathrm{R}_y\mathrm{F}_y}$	$0.32\sqrt{E/R_yF_y}$
Webs of doubly symmetric rolled and built-up I-shaped sections	h/t_w	$1.49\sqrt{E/F_y}$	For $C_a \le 0.114$ $3.96\sqrt{\mathrm{E}/\mathrm{R}_y\mathrm{F}_y}(1-3.04C_a)$ For $C_a > 0.114$ $1.29\sqrt{\mathrm{E}/\mathrm{R}_y\mathrm{F}_y}(2.12-C_a)$ $\ge 1.57\sqrt{E/R_yF_y}$ where $C_a = P_u/\varphi_c P_y$ (LRFD)	For $C_a \le 0.114$ $2.57\sqrt{E/R_yF_y}(1-1.04C_a)$ For $C_a > 0.114$ $0.88\sqrt{E/R_yF_y}(2.68-C_a)$ $\ge 1.57\sqrt{E/R_yF_y}$ where $C_a = P_u/\varphi_c P_y$ (LRFD)

[a] AISC [1]

[b] AISC [2]

of special moment frames. The experimental parameters are flange and equivalent web slenderness ratios, i.e. $b/2t_f$ and $(h/t_w)_{eq}$. The parameter $(h/t_w)_{eq}$ is the web slenderness ratio of the full W24 section, where the depth is three times that of the T-section member. Changing $(h/t_w)_{eq}$ changes the amount of web restraint applied to the flanges. To achieve control over the slenderness ratios, built-up sections were preferred over cutting T-sections from an existing W-sections. The effect of residual stress due to the welding between the web and flange is considered insignificant as the specimens undergo large plastic deformations. To confirm that the test results from built-up T-section specimens are transferable to WT-section members, a WT-section specimen cut from a W-section member with similar slenderness ratios to one of the built-up T-section specimens is also studied.

Five flange thicknesses and three web thicknesses are selected to cover a range of local slenderness ratios. The employed built-up T-section specimens are listed in Table 1, where F1 and W1 represent the thickest flange and web used in the test, respectively, and F5 and W3 represent the thinnest ones. The local slenderness ratios of the specimens are shown in Fig. 3 along with the code-specified limiting ratios for highly ductile (λ_{hd}), moderately ductile (λ_{md}), and non-slender (λ_r) elements, as listed in Table 2. According to AISC [1][2], highly/moderately ductile members are “intended to withstand significant plastic rotation of 0.04/0.02 rad or more” during the design earthquake, and non-slender sections are “cross sections possessing plate components where local buckling in the elastic range will not occur”. Note that only non-slender limits for built-up sections consider the effect of web slenderness ratio on flange capacity by using the k_c factor, where k_c is the buckling coefficient for unstiffened elements and is calculated as $4/\sqrt{h/t_w}$.

The built-up T-section and WT-section specimens were made of ASTM A572 Gr. 50 steel and A992 steel, respectively. The steel was ordered in two batches, and two coupons were taken from each plate in each batch and tested in accordance with ASTM E8 [21]. Table 3 summarizes the average material properties of the two coupons from each batch of material.

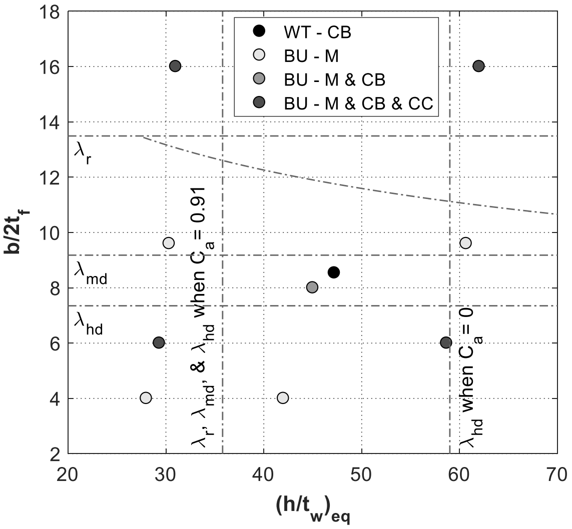

Fig. 3. Local slenderness ratios of specimens along with code-specified limiting ratios for highly ductile (λ_{hd}), moderately ductile (λ_{md}), and non-slender (λ_r) elements. WT: WT sections. BU: built-up section

Table 3. Results of Tensile Coupon Tests.

Material	t (mm)	Batch 1			Batch 2		
		F_y (MPa)	F_u (MPa)	Elongation (%)	F_y (MPa)	F_u (MPa)	Elongation (%)
A992	9.65	357	470	39.8	381	481	49.9
	5.84	360	475	35.6	400	487	42.0
A572	19.1	357	506	36.2	380	540	-
	12.7	380	460	40.5	407	464	36.9
	9.53	414	469	41.7	401	465	54.9
	7.94	440	484	31.3	471	537	42.3
	6.35	425	470	27.6	365	448	48.3
	4.76	408	513	29.2	368	496	36.9

The specimens are tested using the setup shown in Fig. 4. The web plate is welded to the flange plate using a 2-sided fillet weld to form the built-up specimens. The specimens are then welded to fixture plates that are bolted to the fixed loading heads of a 2.22 MN uniaxial hydraulic load frame. Axial loading is applied in displacement control. The applied axial load is directly measured by a load cell, while the axial displacement is measured by an optical tracking system with the markers located at the center and four edges of the fixture plates. The five measured relative axial displacements were averaged to obtain only the deformation in the specimen.

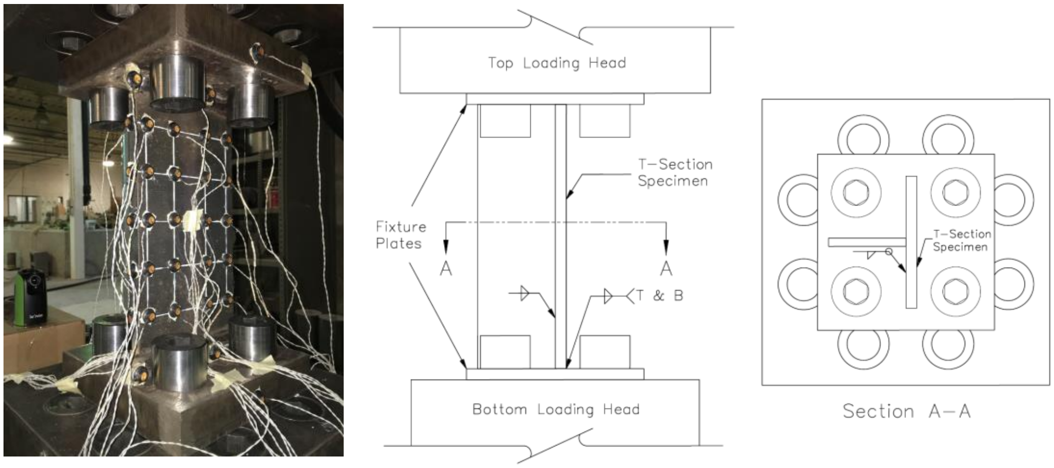

Fig. 4. Test setup.

4.2 Loading schemes

Three different loading protocols are employed in the experiment: (1) monotonic axial compression (designated M); (2) cyclic axial loading that is intended to approximate the seismic demands on flanges in beams (designated CB); and (3) cyclic axial loading intended to approximate the seismic demands on flanges in columns (designated CC). The monotonic loading scheme is used to obtain the buckling and post-buckling capacity of the cross-section without cyclic degradation. The cyclic loading schemes reflect the axial demands on beams and columns under the symmetric cyclic drift loading specified in the AISC seismic provisions [2].

It is assumed that the overall strain distribution across the cross-section of a beam is linear about the neutral axis and that the neutral axis location does not fluctuate with cyclic loading. For a plastic hinge rotation, θ, the flange is subjected to an axial deformation $\Delta = d\theta/2$ in the plastic hinge region, where d is the section depth. Assuming that the plastic hinge length is d [20], then the flange is subjected to a NAD = $\Delta/L = d\theta/2d = \theta/2$ in the plastic hinge region. As a result, the NAD protocol applied to the T-section member, i.e. the CB protocol, is half the beam rotation specified in the beam-column connection qualification protocol. For example, NAD = 2% when a beam achieves 4% plastic rotation, a limit commonly associated with highly ductile response. The resulting CB protocol is shown in Fig. 5.

The existence of axial force in columns increases the severity of web local buckling in column members and causes the columns to shorten under cyclic loading. To take this into account, the CC protocol is developed using finite element simulations of deep column specimens 1L (W24×176), 2L (W24×131), and 3L (W24×104) tested in Ozkula et al. [22] and subjected to symmetric cyclic drift loading. The three columns specimens are subjected to a constant axial load of $0.18P_y$. The computed axial demand histories are averaged and smoothed to get the CC loading protocol shown in Fig. 5. The NAD corresponding to a column drift of 4% in the selected CC protocol is 8.3%. Although this protocol is specific to certain column sizes (similar to those considered in this research) and may not be applicable to other columns, it reflects the flange behavior commonly seen in experimental column tests.

The loading rate for monotonic loading (M protocol) is 1.52 mm/min. Faster rates of 3.05 mm/min for small deformations and 12.2 mm/min for 4% NAD or larger are used for the cyclic loading tests (the CB and CC protocols) to reduce test duration to a reasonable time.

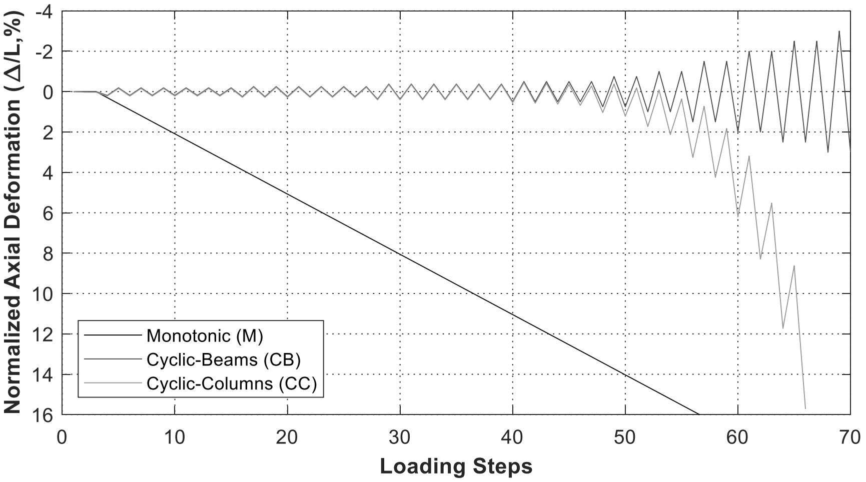

Fig. 5. Employed loading schemes.

5. Experimental Results

5.1 Comparison between WT-Section and T-Section Specimens

Fig. 6 shows a comparison between the hysteresis responses and backbone curves of a WT-section (W12×26) and a T-section (F3W2) specimen with similar slenderness ratios subjected to the CB loading protocol. Except for the sudden drop in the backbone curve under tension due to a lapse of applying axial displacement, Fig. 6 clearly shows that both specimens yield generally similar responses in terms of peak load, post-buckling strength, post-peak degradation rate and hysteresis under cyclic loading. This comparison provides confidence in the use of built-up sections in this study and suggests that the findings also can be applied to W-sections.

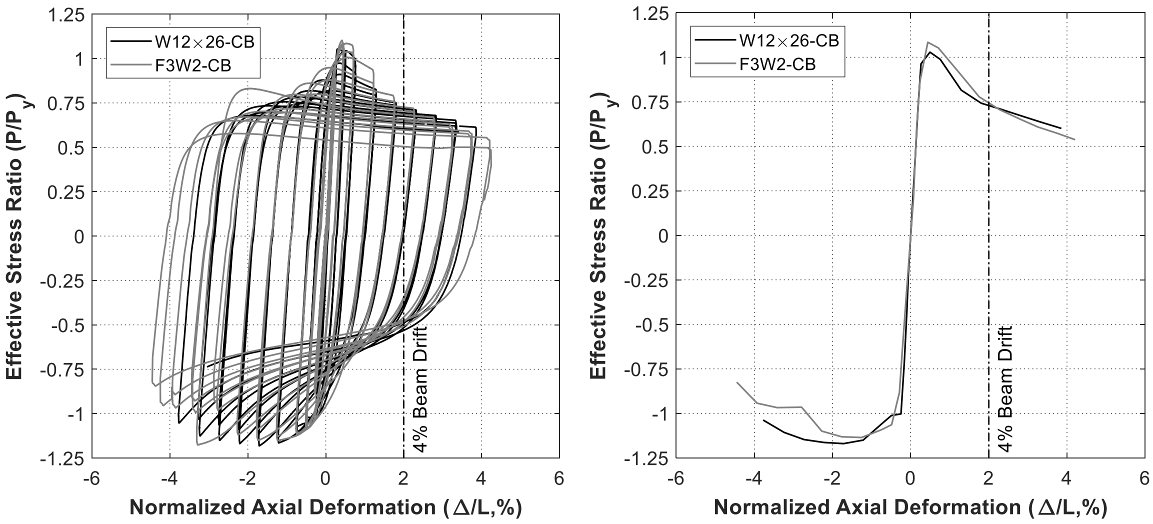

(a) (b)

Fig. 6. Comparison of (a) hysteresis responses and (b) backbone curves for WT-section and T-section specimens with similar slenderness ratios under the CB protocol

5.2 FLB Modes

The specimens subjected to both monotonic and cyclic loading exhibit two distinct buckled shapes, asymmetric and symmetric FLB, as shown in Fig. 7(a, d) and (b, e), respectively. The buckling mode of each specimen is documented in Table 1. Most of the specimens exhibit asymmetric buckling behavior, where the flange and web interact with each other and experience local buckling simultaneously. The test data indicates that specimens that have comparable flange and web slendernesses are more likely to experience asymmetric buckling.

A few specimens with a very stocky flange and a slender web, e.g. Specimen F1W2 with $b/2t_f$ of 4.0 and $(h/t_w)_{eq}$ of 42.0, buckle in a symmetric mode, i.e. both half flanges bend together in the direction of the plane of the web, as shown in Fig. 7(b). In this case, the flange itself suffers from weak-axis flexural buckling because the restraint provided by the web is relatively minimal and not able to alter the flange buckling mode. Within the studied range of slenderness ratios, only the specimens with $b/2t_f \leq 6$ are susceptible to this mode.

The asymmetric buckling behavior is commonly seen in plastic hinge zones of deep columns subjected to combined axial and lateral loading [22][23], lending credence to the premise of this paper, i.e. the T-section specimens can replicate certain flange buckling responses and be used to study the flange behavior in plastic hinge regions under large lateral displacements. The symmetric buckling behavior has also been seen in previous tests [24], but with slight flange-web junction displacement and in columns with the extreme combination of a stocky flange and a very stocky web, e.g. W14×176 with $b/2t_f = 5.97$ and $h/t_w = 13.7$.

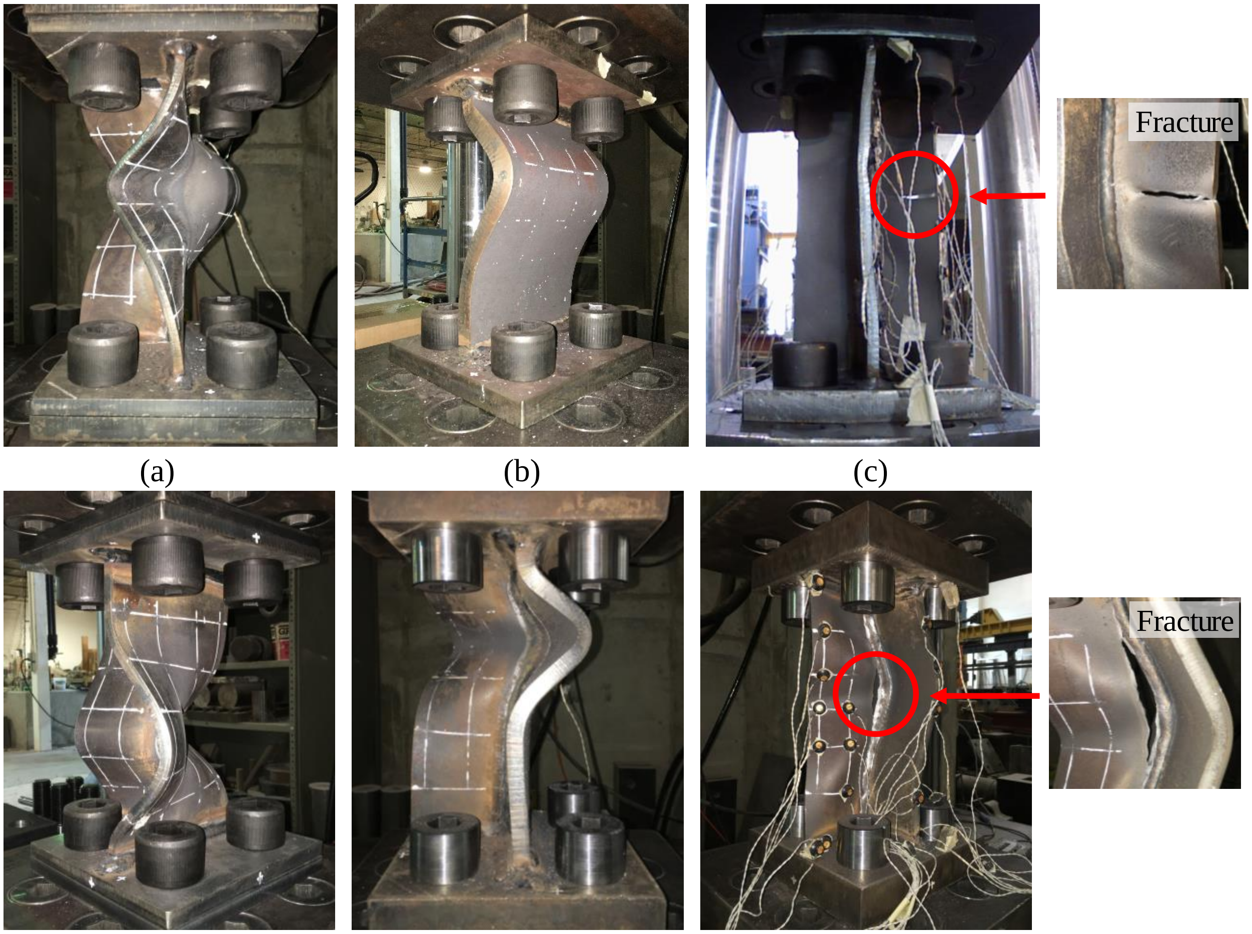

(a) (b) (c)

(d) (e) (f)

Fig. 7. Asymmetric local buckling in (a) Specimen F4W3-M and (d) Specimen F3W2-M; symmetric local buckling in (b) Specimen F1W2-M and (e) Specimen F2W1-CC; and fracture in (c) Specimen F2W1-CB and (f) Specimen F2W3-CB.

5.3 Response under Monotonic Loading

The nine specimens under monotonic loading are compressed to 10% NAD and ESR is computed using the material yield strength obtained from the coupon tests listed in Table 3. The ESR versus NAD curves of the nine T-section specimens are plotted in Fig. 8, where specimens with the same flange thickness are plotted in the same color, while the specimens with the same web thickness are plotted in the same line style.

By comparing the curves of the specimens with a web thickness of 9.5 mm, i.e. W1 specimens plotted as solid curves, it is clear that the smaller the $b/2t_f$, the higher the buckling and post-buckling strength. For example, specimen F1W1-M's peak strength reaches $1.24P_y$ ($b/2t_f = 4.0$), meanwhile as $b/2t_f$ increases, the buckling strength drops to $1.18P_y$, $1.07P_y$, and $1.02P_y$ for F2W1-M, F4W1-M, and F5W1-M, respectively. All four W1 specimens can reach P_y even though F5W1-M has a $b/2t_f = 16.0$, which is larger than $\lambda_r = 13.5$. The better than expected performance results from the fixed end condition, which causes a full buckling wavelength that is commonly seen in experiments and simulations [13, 24], unlike the pinned end conditions conservatively assumed in the AISC specification [1]. In terms of post-buckling capacity, λ_{hd} works well for identifying the sections with superior ductility. Specimens with a $b/2t_f$ lower than $\lambda_{hd} = 7.35$, i.e. F1W1-M and F2W1-M, maintain a large post-buckling capacity of at least P_y until 8.9% and 4.5% NAD, respectively, which are much higher than NAD = 2% that corresponds to 4% beam drift. On the other hand, F4W1-M and F5W1-M that have a $b/2t_f$ larger than λ_{hd} exhibit rapid strength degradation after reaching the peak values and can only maintain P_y up to NADs of 0.8% and 0.7%, respectively.

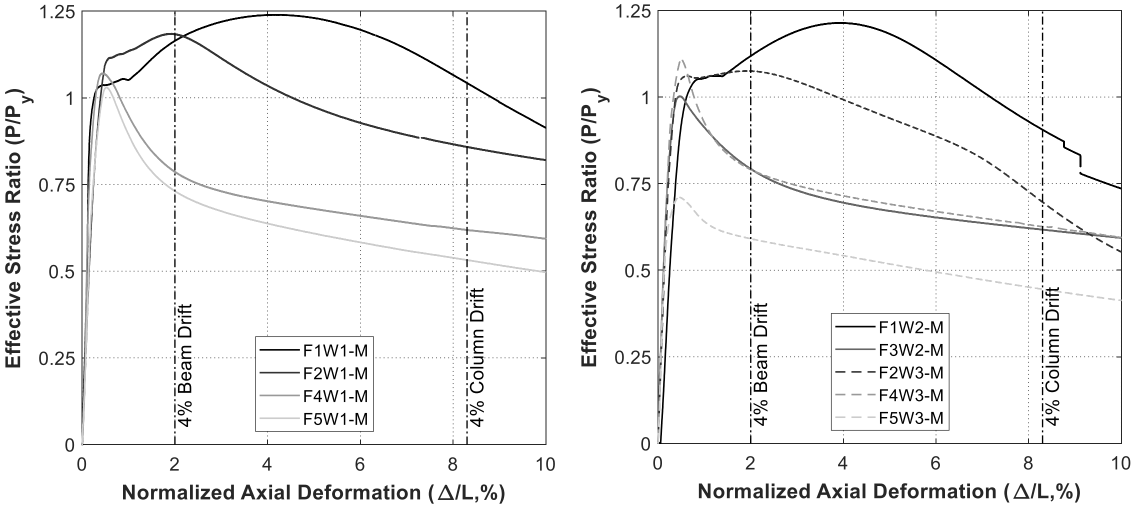

(a) (b)

Fig. 8. Effective stress ratio-normalized axial deformation curves of specimens under monotonic axial compression: (a) W1 specimens; (b) W2 and W3 specimens

The effect of equivalent web slenderness ratio, $(h/t_w)_{eq}$, on flange behavior is not significant when $b/2t_f$ is smaller than 10 as can be seen from the comparison of specimens F1W1-M, F2W1-M, and F4W1-M to their counterparts with slenderer webs, i.e. F1W2-M, F2W3-M, and F4W3-M. For specimens with slender flanges, e.g. F5W1-M and F5W3-M, the effect of $(h/t_w)_{eq}$ is significant because the slender flange negatively interacts with the slender web. As shown in Fig. 8, while Specimen F5W1-M has a peak strength of $1.02P_y$, F5W3-M reaches an axial capacity of only $0.7P_y$. Overall, for flanges under monotonic compression, the λ_r and λ_{hd} limits in current seismic provisions seem to be reasonable.

5.4 Effects of Cyclic Loading

The resulting relationship between ESR and NAD of the specimens under the three applied loading protocols are plotted together in Fig. 9. Positive and negative NAD represent compression and tension, respectively, to be consistent with Fig. 8.

Although the difference in peak compression strength between specimens under the M and CB protocol is not significant, the degradation rate of post-buckling compression strength of the specimens subjected to CB demands is considerably faster than their monotonic counterparts. For example, as shown in Fig. 9(c), while Specimen F2W1-M maintains an axial capacity of at least P_y up to 4.5% NAD, Specimen F2W1-CB can only sustain P_y to 1.5% NAD and quickly degrades to $0.85P_y$ at 2% NAD, suggesting that moment capacity of beams satisfying the λ_{hd} limits starts to degrade after reaching 3% drift. The effect is even more pronounced for Specimen F2W3-CB. These results suggest that the web restraint has a large impact on the rate of degradation with continued cycling to large NAD levels. The strength degradation rates for specimens with high $b/2t_f$, e.g. specimen F5W1-CB and F5W3-CB, are comparable to their monotonic counterparts before 2% NAD. After reaching 2% NAD, the rate of degradation is much faster. For example, the post-buckling strength of both specimens under the CB protocol is $0.51P_y$ and $0.44P_y$ at 3% NAD, respectively, compared to $0.67P_y$ and $0.57P_y$, respectively, under monotonic loading.

Degradation of tensile strength occurs with cyclic loading, but the rate is substantially smaller than that under compression. Tensile degradation generally begins during the 1.5% or 2% NAD cycles. Specimens typically fail when the tensile strength drops to $0.8P_y$. Failure occurs due to fracture, as marked by red circles in Fig. 9. One key characteristic that slenderness ratios influence is the recovery of the tensile strength after unloading from compression. Specifically, more tensile strain is required to stretch out the buckled shape and recover tensile strength for specimens that have higher $b/2t_f$ and $(h/t_w)_{eq}$, i.e. experience more severe local buckling. For example, during the 2% NAD cycle, Specimen F2W1-CB can reach $0.8P_y$ at 0.7% NAD, but Specimen F5W3-CB has to be pulled to -1.3% NAD (tension side) to recover the same level of tensile strength, as shown by the red (thicker) lines in Fig. 9(c) and (b).

Although specimens under the CB protocol have the same buckled shape as the ones under the M protocol, they eventually failed by ultra-low-cycle fatigue under tension. As shown in Fig. 7(c), for Specimen F2W1-CB, fracture initiates at midpoints along the outer edges of the flange and web, where the highest strain level occurs due to the buckling behavior. Because of the connection between strain level and buckling behavior, fracture occurs earlier for specimens with larger $b/2t_f$ and $(h/t_w)_{eq}$ due to buckling during earlier cycles. For example, fracture occurs during the 3.5% NAD cycle for Specimen F5W3-CB and is delayed to the 4.5% and 5.5% NAD cycles for Specimens F5W1-CB and F2W1-CB, respectively. One exception is that Specimen F2W3-CB suffers from earlier fracture at the midpoint along the flange-web connection during the 3% NAD cycle due to symmetric buckling behavior, as shown in Fig. 7(f), suggesting that buckling mode also has an influence on fracture behavior. Although ultra-low-cycle fatigue is the eventual failure mode for all specimens, severe strength degradation under compression occurred much earlier and therefore is a design concern.

The responses of the four specimens under the CC protocol are shown in Fig. 9. The backbone curves of the F5 specimens are almost identical to the responses of their monotonic counterparts. The F2 specimens under the CC protocol, unlike their monotonic counterparts, buckle in a symmetric mode and have a lower backbone curve. From Fig. 9 it can be seen that all specimens under the CC protocol experience much less tensile plastic strain than specimens under the CB protocol, allowing the specimens to deform to greater NADs without succumbing to ductile fracture. Nevertheless, the ESR of the specimens under the CC protocol at the 8.3% NAD that corresponds to 4% column drift is lower than that of the specimens under the CB protocol at the 2% NAD that corresponds to 4% beam drift, as can be observed from Fig. 9. For example, the ESR of F2W1-CC at the 8.3% NAD and F2W1-CB at the 2% NAD is 0.78 and 0.85, respectively. These lower ESRs may greatly degrade column capacity and require further investigation.

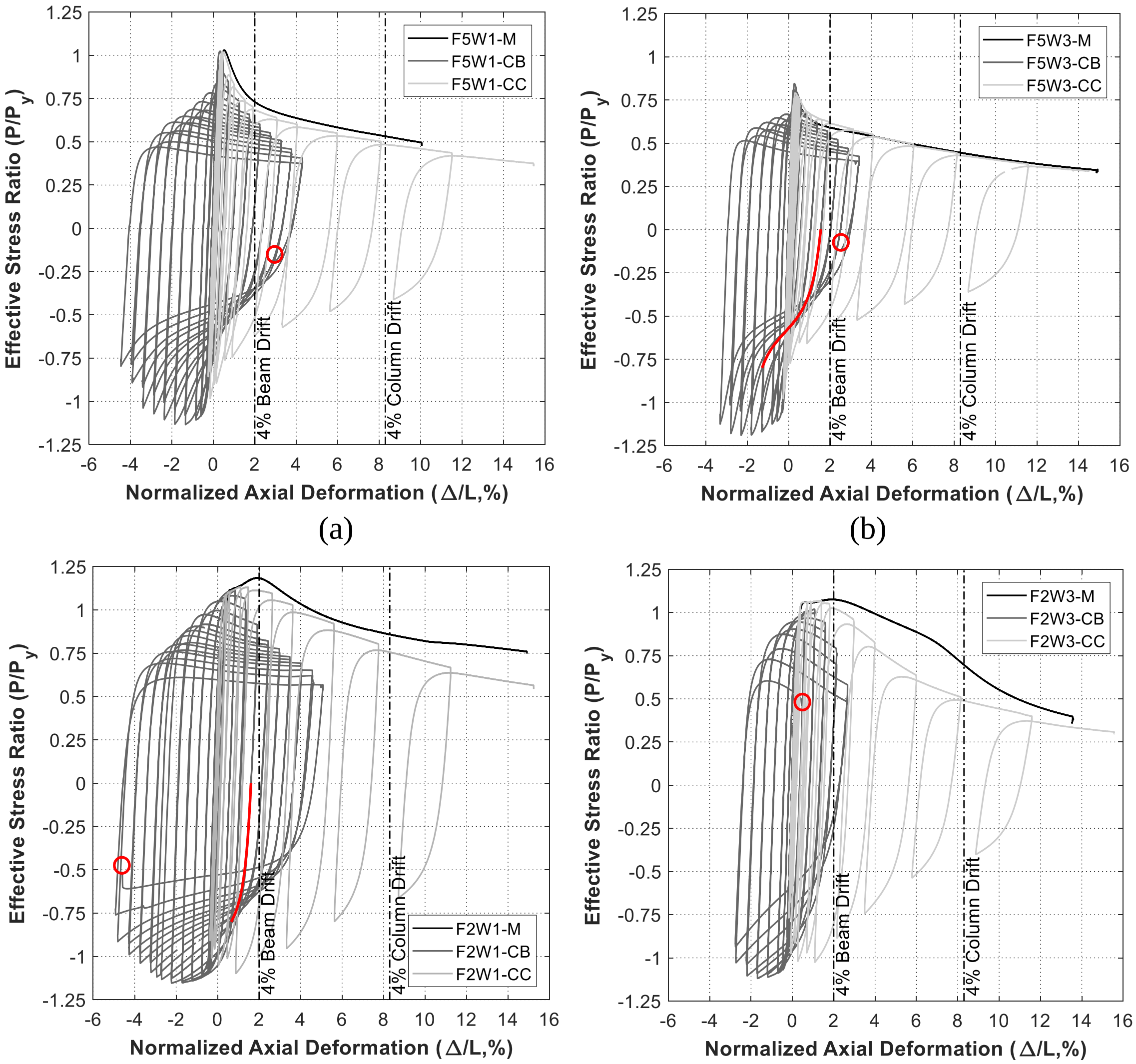

(a) (b)

(c) (d)

Fig. 9. Comparison of axial force ratio-axial strain curves between different loading schemes for Specimen (a) F5W1; (b) F5W3; (c) F2W1; and (d) F2W3.

6. Finite Element Simulations

Computational simulation is used to expand the parameter space and gain greater insight into the effects of FLB on member capacity.

6.1 Validation

In addition to the validation effort discussed earlier in the paper, the modeling approach is further validated using the experimental data presented in Section 5. Due to limited space, only a comparison of responses of Specimen F3W2-M and F5W1-CC are shown in Fig. 10. The measured specimen dimensions and material properties obtained from tensile coupon tests in Table 3 are used in the finite element simulation. The peak strength, post-buckling strength, cyclic strength degradation rate obtained from the simulation match well with those measured during the physical testing and provide additional confidence that the employed modeling techniques can generate reasonable behavior.

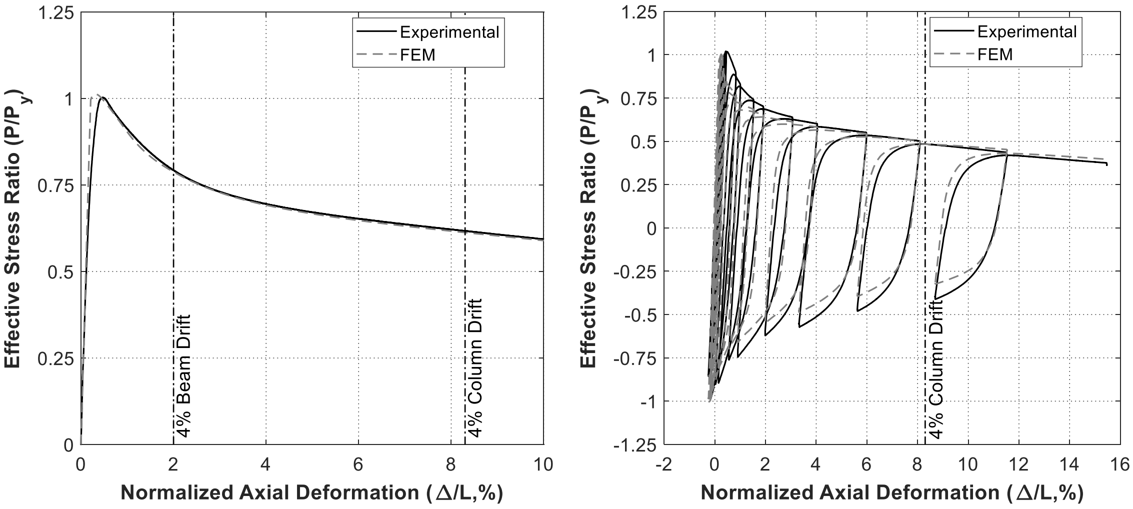

(a) (b)

Fig. 10. Comparison of responses between experimental and simulation results for Specimen (a) F3W2-M and (b) F5W1-CC.

6.2 Section Selection and Performance Parameter

To study the effect of slenderness ratio on cyclic capacity of column flanges, finite element models of T-sections with *b* = 152.4 mm, *d*/3 = 101.6 mm, and $b/2t_f$ and $(h/t_w)_{eq}$ ranging from 6 to 16 and 24 to 56, respectively, are created using the modeling approach described in Section 2. The values of *b* and *d* are the same as the tested specimens, and the range of slenderness ratios is selected to cover most commercial standard W-section sections. The T-section models are axially loaded according to the CC protocol to further study the lower ESRs observed from these specimens.

In all simulation cases, ESR is used to track cross-section capacity at different column drift levels. As noted earlier, column drift levels are gauged from detailed finite element analysis of entire columns. Fig. 11 shows the results of a T-section where $b/2t_f$ = 6 and $(h/t_w)_{eq}$ = 32. The ESR is 0.94, 0.83, 0.76 and 0.69 at column drift levels of 1%, 2%, 3%, and 4%.

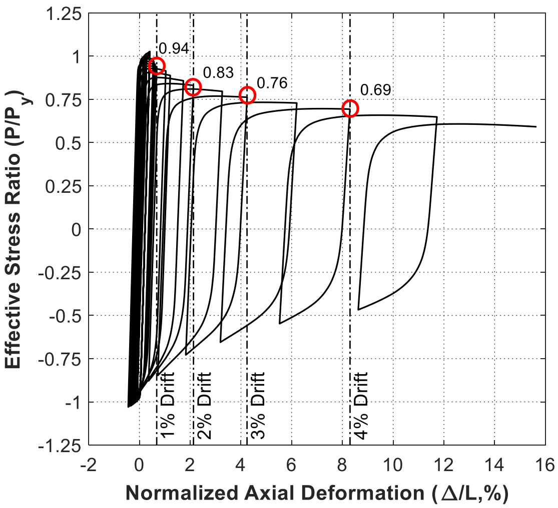

Fig. 11. The effective stress ratio (ESR) corresponding to different column drifts for the T-section with $b/2t_f$ = 6 and $(h/t_w)_{eq}$ = 32 under the CC protocol.

6.3 Simulation Results

All T-sections buckle in the asymmetric mode with the ESRs plotted in Fig. 12 against $b/2t_f$ for column drift levels of 1% through 4% for different values of $(h/t_w)_{eq}$. It is clear that $(h/t_w)_{eq}$ has a negative effect on ESR. While the negative effect is significant when the drift level is small, 1%, it diminishes as both $(h/t_w)_{eq}$ and drift level decrease in value. The effect also diminishes as the value of $b/2t_f$ decreases. The above results further confirm the trend observed from the tests: the effect of $(h/t_w)_{eq}$ is significant only on post-buckling strength at small strain levels when the flange is slender. An important observation from Fig. 12(d) is that the ESR curves tend to cluster together at drift levels in excess of 2%, suggesting that it is reasonably accurate to ignore the effect of $(h/t_w)_{eq}$ on λ_{hd} limits for the flanges.

Fig. 12 also shows that both $b/2t_f$ and drift level adversely affect ESR. For example, for T-sections with $(h/t_w)_{eq} = 56$, the ESR corresponding to 1% drift decreases from 0.92 to 0.61 when $b/2t_f$ increases from 6 to 16. ESR drops significantly as the column drift increases to 4%, where its range decreases from 0.92 - 0.61 to 0.70 - 0.50 for $b/2t_f$ ranging from 6 to 16. Through a regression analysis, the effect of $b/2t_f$ and drift level on ESR can be quantified by the following bilinear equation with $b/2t_f = 8$ as a transition point:

$$\begin{aligned} ESR &= (0.0575 - 0.422DR)\left(23.3 - \frac{b}{2t_f}\right) \text{ for } 6 \le \frac{b}{2t_f} \le 8 \\ ESR &= (0.0205 - 0.15DR)\left(51 - \frac{b}{2t_f}\right) \text{for } 8 < \frac{b}{2t_f} \le 16 \end{aligned} \qquad (1)$$

where DR is the column drift ratio, e.g. 0.04 rad for the cases in Fig. 12(d). Equation (1) is plotted as the solid black line in Fig. 12 and portrays the negative effect of both $b/2t_f$ and drift level on ESR. Another observation is that the degradation of ESR with drift level could be substantial.

According to Equation (1), when $b/2t_f=\lambda_{hd}$, ESR drops from 0.78 to 0.65 (17% decrease) as *DR* increases from 2% to 4%.

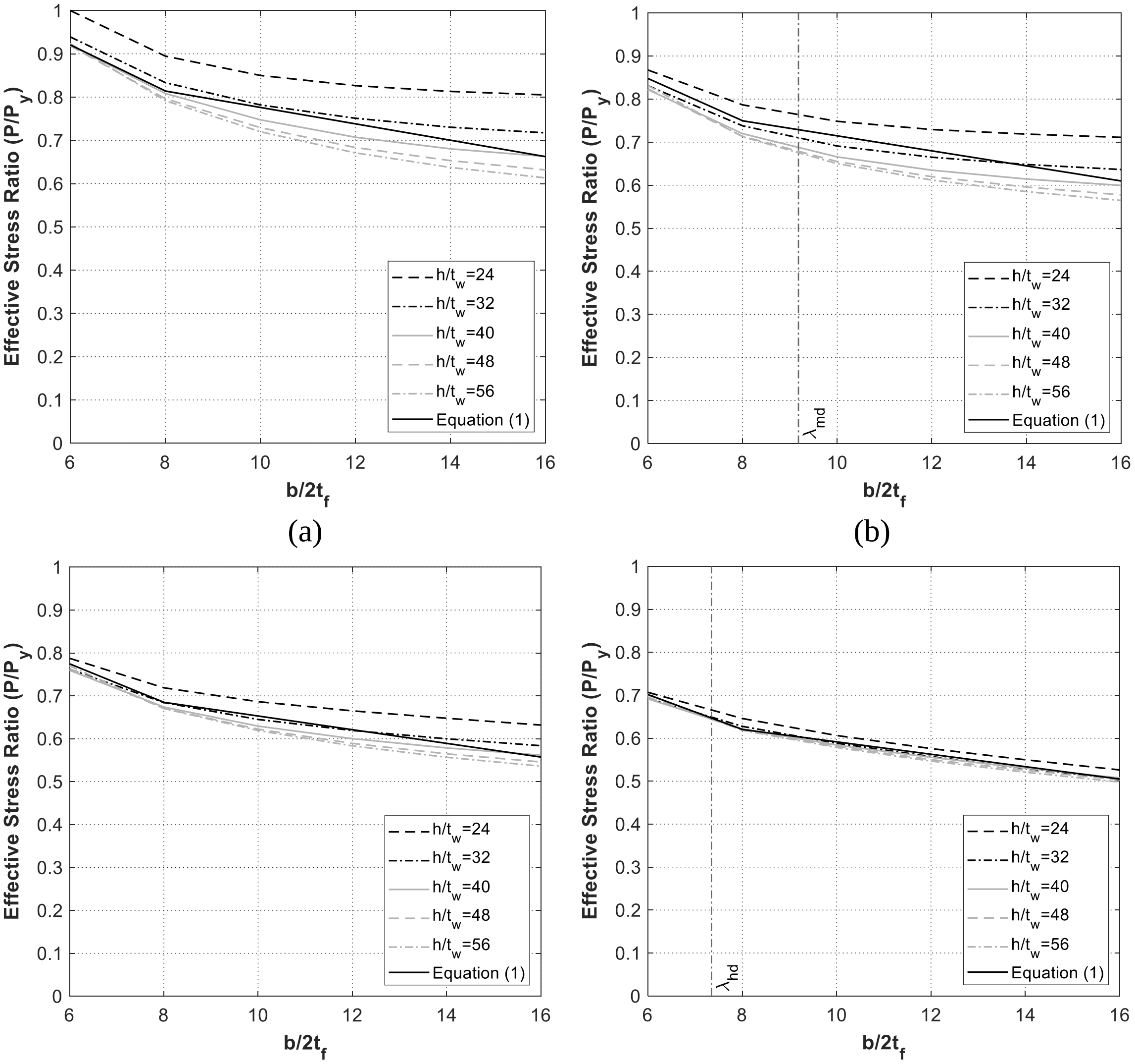

(a) (b)

(c) (d)

Fig. 12. Effective stress ratio (ESR) of T-sections at column *DR* of (a) 1%; (b) 2%; (c) 3% and (d) 4%.

7. Comparison with Current AISC Seismic Provisions

All specimens with $b/2t_f$ and $(h/t_w)_{eq}$ smaller than λ_r have a buckling strength larger than P_y under all loading schemes. Even when $b/2t_f$ exceeds λ_r, e.g. F5W1 specimens, a peak strength of at least

P_y is still achieved. While not shown in this paper, the computational study also supports this finding. As a result, the current λ_r limit is considered adequate for flanges in beams and columns under the monotonic and cyclic loading schemes considered in this work.

From the experimental results, it is also clear that λ_{hd} is reasonable under monotonic loading. This assessment is based on the observed good post-buckling responses exhibited by monotonically loaded specimens with F1 and F2 flanges. The same can be said for specimens subjected to cyclic axial loading for demands under the CB protocol. The degradation in tensile strength is much milder than the post-buckling degradation seen under compression, which combined, will likely allow most available cross-sections to carry at least 80% of their plastic moment capacity up to 4% rotation. Therefore, current limits on λ_{hd} for flanges appear to provide appropriate highly ductile behavior for beams under cyclic loading.

Specimen F2W1-CC, which has a $b/2t_f$ smaller than the current λ_{hd} limit, exhibits an ESR of $0.78P_y$ at a NAD corresponding to 4% column drift. Equation (1) indicates that ESR reaches 0.65 at the highly ductile slenderness limit. The evidence in this paper suggests that, barring other failure modes such as global instability, a W24 column with slenderness characteristics similar to those considered would be able “to withstand significant plastic rotation of 0.04 rad or more” per current design philosophy and still support a substantial axial load. However, the key question of whether the moment or axial capacities have been degraded too much by cyclic FLB is not addressed in current seismic provisions. Unlike beams, where current seismic design provisions require that the moment capacity be at least 80% of the plastic capacity at 4% drift, columns have no such requirement. The research in this paper points out the need for more precise performance requirements for columns.

8. Conclusions

The effect of cyclic FLB on the capacity of structural members in special moment frames was experimentally and computationally investigated in this study. Nineteen half-scale T-section specimens were axially loaded to represent the flange/web subassembly in the plastic hinge region of a wide flange section under combined axial and flexural loading. The specimens were selected to cover a wide range of slenderness ratios and subjected to three different loading schemes. The loading schemes included monotonic compression, meant to obtain the flange capacity without cyclic degradation, and two cyclic axial loading histories, one that reflected the axial demands on beam flanges and another for column flanges under cyclic drift loading. To further study the cyclic behavior of column flanges and justify the observation from the test results, a parametric computational study with different slenderness ratios was performed. The effect of slenderness ratios on column compression capacity due to flange strength degradation was then evaluated.

The test results showed that most T-section specimens could reach a peak strength of P_y regardless of the value of $b/2t_f$, but $b/2t_f$ substantially influenced post-buckling behavior. Under monotonic loading, the current value for λ_{hd} for a flange was shown to be a boundary between large buckling capacity and rapid degradation after reaching peak strength. The effect of $(h/t_w)_{eq}$, on the other hand, was shown to be secondary and became significant only when both $b/2t_f$ and $(h/t_w)_{eq}$ were large and negatively interacted with each other.

Specimens under the CB loading protocol exhibited much more severe compressive strength degradation than the monotonic protocol. Depending on a specimen's $b/2t_f$, the compressive strength dropped to as low as 0.53 P_y at deformation levels that corresponded to 4% beam rotation. The tensile strength had a much milder degradation rate than the compressive strength. However, the required tensile strain for recovery of tensile strength after unloading from compression depended on the slenderness ratio due to the effort of stretching out the buckled shape.

The backbone curves of specimens under CC loading were much higher than those for specimens under CB loading and were quite close to the responses under M loading. This result was attributed to the smaller tensile plastic strain demands and led to a milder cyclic degradation rate under compression. Nevertheless, the degradation at higher drift levels could be substantial and could compromise the axial and flexural capacities of the columns.

The experimental and computational data was used to evaluate the current AISC seismic provisions. It was shown that the current λ_r limit is adequate for flanges in beams and columns under the monotonic and cyclic loading schemes considered in this work. It was also shown that λ_{hd} is reasonable for members under monotonic loading and CB loading, which is representative of the demands seen in beams. The conclusion for λ_{hd} and λ_{md} under CC loading, representative of the demands seen in columns, was not definitive because the performance expectations of the AISC seismic provisions are not as explicit as they are for beams. The research outlined in this paper provides useful input to refine current specifications to address this issue.

The evaluation in this paper is only valid for the specific wide flange section sizes, loading protocols and range of parameters studied. Although this research points out specific drawbacks in the current AISC seismic provisions, additional research is needed to broaden the results and draw comprehensive conclusions that warrant specification changes.

Acknowledgements

This work was supported by the University of Michigan and US NSF grant number ACI-1638186. Any opinions, findings, conclusions, and recommendations expressed in this paper are those of the authors and do not necessarily reflect the views of the sponsor.

References

[1] ANSI/AISC 360-16 Specification for Structural Steel Buildings. Chicago, IL: American Institute for Steel Construction; 2016.

[2] ANSI/AISC 341-16 Seismic Provisions for Structural Steel Buildings. Chicago, IL: American Institute for Steel Construction; 2016.

[3] Sawyer HA. Post-Elastic Behavior of Wide-Flange Steel Beams. Journal of the Structural Division ASCE 1961; 87 (ST8): 43–71.

[4] Lay MG. Some Studies of Flange Local Buckling in Wide-Flange Shapes. Journal of the Structural Division ASCE 1965; 91(6): 94-116.

[5] Bansal JP. The Lateral Instability of Continuous Steel Beams. CESRL Dissertation No. 71-1. Austin, TX: University of Texas; 1971.

[6] Kemp AR. Factors Affecting the Rotation Capacity of Plastically Designed Members. Struct Eng 1986; 64B(2): 28-35.

[7] Richards PW, Uang C-M. Effect of flange width-thickness ratio on eccentrically braced frames link cyclic rotation capacity. J Struct Eng ASCE 2005; 131(10): 1546–1552.

[8] Newell JD, Uang C-M. Cyclic behavior of steel wide-flange columns subjected to large drift.” J Struct Eng ASCE 2008; 134(8):1334-1342.

[9] Cheng X, Chen Y, Nethercot DA. Experimental study on H-shaped steel beam-columns with large width-thickness ratios under cyclic bending about weak-axis. Eng Struct 2013; 49: 264-274.

[10] Elkady A, Lignos DG. Analytical investigation of the cyclic behavior and plastic hinge formation in deep wide-flange steel beam-columns. Bull Earthquake Eng. 2015; 13: 1097-1118.

[11] Fogarty J, El-Tawil S. Collapse resistance of steel columns under combined axial and lateral loading. J Struct Eng ASCE 2015; 142(1): 04015091.

[12] Fogarty J, Wu T.-Y., El-Tawil S. Collapse Response and Design of Deep Steel Columns Subjected to Lateral Displacement. J Struct Eng ASCE 2017; 143(9): 04017130

[13] Wu T-Y, El-Tawil S, McCormick J. Highly ductile limits for deep steel columns. J Struct Eng ASCE 2018; 144(4): 04018016.

[14] Altair Computing. Hypermesh Version 12.0. Troy, MI: Altair Engineering Inc.; 2013.

[15] Hallquist J. LS-DYNA. Livermore, CA: Livermore Software Technology Corp; 2013.

[16] Engelmann BE, Whirley RG, Goudreau GL. A simple shell element formulation for large-scale elastoplastic analysis. In: Noor AK, Belytschko T, and Simo JC, editors. Analytical and computational models of shells. New York: ASME, New York; 1989.

[17] Huang Y, Mahin SA. Simulating the inelastic seismic behavior of steel braced frames including the effects of low-cycle fatigue. Rep. No. PEER 2010/104. Berkeley, CA: Pacific Earthquake Engineering Research Center, Univ. of California at Berkeley; 2010.

[18] Arasaratnam P, Sivakumaran KS, Tait MJ. True stress-true strain models for structural steel elements. ISRN Civ Eng 2011. http://dx.doi.org/10.5402/2011/656401

[19] Wu T-Y, El-Tawil S, McCormick J. Seismic collapse response of steel moment frames with deep columns. J Struct Eng ASCE 2018; 144(9): 04018145.

[20] MacRae GA, Carr AJ, Walpole WR. The seismic response of steel frames. Research Rep. No. 90-6. New Zealand: Dept. of Civil Engineering, Univ. of Canterbury; 1990.

[21] ASTM E8/E8M-15a Standard test methods for tension testing of metallic materials. West Conshohocken, PA: ASTM; 2015.

[22] Ozkula G, Harris J, Uang C-M. Observations from cyclic tests on deep, wide- beam-column columns. AISC Eng. J. 2017; 54(1): 45–61.

[23] Elkady A, Lignos DG. Full-Scale Testing of Deep Wide-Flange Steel Columns under Multiaxis Cyclic Loading: Loading Sequence, Boundary Effects, and Lateral Stability Bracing Force Demands. J Struct Eng ASCE 2017; 144(2): 04017189.

[24] Ozkula G, Harris J, Uang C-M. Classifying Cyclic Buckling Modes of Steel Wide-Flange Columns under Cyclic Loading. Structures Congress 2017: 155-167.